Experimental Investigation on Nonlinear Flexural Behavior of Post-Tensioned Concrete Bridge Girders with Different Grouting Conditions and Prestress Levels

Daniele Losanno[1]; Simone Galano[2]; Fulvio Parisi[3]; Maria Rosaria Pecce[4]; and Edoardo Cosenza[5]

Abstract: In past decades, the occurrence of catastrophic collapses in post-tensioned concrete (PC) bridges in several countries has raised major concerns about their load-bearing capacity, calling for numerical and experimental studies on the effects of aging, deterioration, and construction defects. In order to investigate the influence of residual prestressing levels and the imperfect grouting of ducts in PC bridges, we undertook an experimental study on the flexural behavior of six PC girders prestressed with two monostrand tendons having a nearly parabolic route. The specimens' geometry was properly designed based on a 1:5 length scale, assuming a prototype representative of simply supported, beam-type highway bridges in Italy. Two prestress levels were considered as being representative of the expected and defective post-tensioning levels, as observed in several existing bridges. In combination with a different prestressing level, the specimens' ducts were provided with either full grouting, partial grouting, or no grouting in order to consider the whole range of possible bonding conditions for post-tensioning tendons. The girders were tested in a four-point bending configuration under a quasi-static cyclic protocol up to force-based performance levels, followed by a monotonic loading protocol with displacement control up to failure. The different impacts of the prestress level and grouting condition were addressed in terms of the initial (uncracked) behavior, post-cracking behavior, and ultimate capacity. Limited serviceability was achieved in the case of lower prestressing levels, while a 12% to 15% lower load-bearing capacity was attained in the case of unbonded tendons. In the last section of the paper, an analytical study on the initial stiffness and moment–curvature behavior is discussed in support of the interpretation of the experimental findings. **DOI: 10.1061/JBENF2.BEENG-6466**.

Author keywords: Prestressed concrete bridges; Defective grouting; Residual prestress; Experimental tests; Analytical prediction; Beam-type bridges.

Introduction

Post-tensioned concrete (PC) bridges are the most common type of existing bridges erected in Italy before the 1980s (Borzi et al. 2015; Cosenza and Losanno 2021). The performance of PC structures has been observed to be greatly affected by degradation phenomena and construction defects in the post-tensioning tendons and their surrounding ducts. In Italy, approximately 18% of bridge collapses have been found to be caused by human error in their design or construction (approximately 11%) and degradation of their structural components (approximately 7%). These statistics are in line with data on bridge collapses that occurred in the US between 1989 and 2000 (Anitori et al. 2013; Cook et al. 2015; Deng et al. 2016; Wardhana et al. 2003).

After the disaster of the Polcevera Bridge in Genova, Italy, in 2018 (Nuti et al. 2020), Italian guidelines were issued for the risk classification, safety checking, and structural health monitoring of existing bridges (MIT 2019), highlighting that PC bridges are among the most vulnerable structures and require in-depth inspections and safety assessments. Along the same lines, the Italian agency for public roadways [i.e., the Azienda Nazionale Autonoma delle Strade Statali (ANAS)] recently issued a reference document for the in-depth inspections of PC bridge decks (ANAS 2020). ANAS bridge stock counts approximately 15,000 bridges, 40% of which consists of beam type post-tensioned concrete decks and was erected between 1955 and 1980.

In the PC construction process using bonded tendons, after the strands have been post-tensioned, the ducts are expected to be grouted to provide: (1) a full bond between the strands and the concrete; and (2) protection for the prestressed steel against the water and chlorides in alkaline environments.

Based on tendon inspections of 10 bridges in Vienna, 76% of all the opened duct locations were found to be completely filled, while the remaining 24% exhibited incomplete injection (VSL International 2002). Available data from the UK have revealed that, in a sample of 447 bridges built between 1947 and 1992, more than

[1]Assistant Professor, Dept. of Structures for Engineering and Architecture, Univ. of Naples Federico II, Via Claudio 21, 80125 Naples, Italy (corresponding author). ORCID: https://orcid.org/0000-0002-6857-8867. Email: daniele.losanno@unina.it

[2]Post-Doctoral Researcher, Dept. of Structures for Engineering and Architecture, Univ. of Naples Federico II, Via Claudio 21, 80125 Naples, Italy. ORCID: https://orcid.org/0000-0001-5832-8592. Email: simone.galano@unina.it

[3]Associate Professor, Dept. of Structures for Engineering and Architecture, Univ. of Naples Federico II, Via Claudio 21, 80125 Naples, Italy. ORCID: https://orcid.org/0000-0002-1374-0732. Email: fulvio.parisi@unina.it

[4]Full Professor, Dept. of Structures for Engineering and Architecture, Univ. of Naples Federico II, Via Claudio 21, 80125 Naples, Italy. ORCID: https://orcid.org/0000-0001-7789-9112. Email: pecce@unina.it

[5]Full Professor, Dept. of Structures for Engineering and Architecture, Univ. of Naples Federico II, Via Claudio 21, 80125 Naples, Italy. Email: cosenza@unina.it

Note. This manuscript was submitted on May 15, 2023; approved on October 20, 2023; published online on December 18, 2023. Discussion period open until May 18, 2024; separate discussions must be submitted for individual papers. This paper is part of the ***Journal of Bridge Engineering***, © ASCE, ISSN 1084-0702.

50% of those inspected were affected by voids and about 12% contained ungrouted tendons (*fib 2001*). A total of 620 tendons were investigated in Japan across 84 bridges erected between 1962 and 1985, resulting in 31% of the tendons being found to have defective grouting ranging from some voids to a lack of grout. In the US, post-tensioned construction dates back to the 1950s and is still commonly used for segmental bridges, with the prestressed I-girder bridge type having been replaced in the mid-1980s due to detailing and grouting problems, which led to severe corrosion damage to the tendons. Recent studies have confirmed that the presence of unwanted voids in post-tensioned tendons is one of the main causes of strand corrosion (Trejo et al. 2009; DOT 2013).

Over the last few decades, although both suppliers and designers have implemented new systems, tests, and procedures to improve the durability and long-term performance of PC structures (Alampalli et al. 2021; Chen et al. 2020; Xu et al. 2021), existing PC bridges still need proper inspections and maintenance, combined with further studies to develop specific-capacity models (Gino et al. 2020).

Corroded PC beams have been investigated in a number of studies to shed light on durability issues and their reduced load-bearing capacity resulting from their decreasing mechanical properties and cross-sectional areas (Franceschini et al. 2022; Granata et al. 2021; Harries 2009; Recupero and Spinella 2019; Vecchi et al. 2021).

A few previous studies on PC beams have addressed the influence of corrosion under different grouting conditions, demonstrating that insufficient grouting leads to both decreased prestressing force and load-carrying capacity (Minh et al. 2007; Wang et al. 2014). Wang et al. (2014) conducted an experimental study on the influence of insufficient grouting on the flexural behavior of 2-m-long beams with small cross-sections ($150 \times 220\ mm^2$ in size) and a horizontal, straight, prestressing tendon that had been completely or partially grouted or lacked grouting. Under a constant magnitude of prestressing action, Wang et al. (2014) found that the postcracking flexural behavior of the beam mainly depended on the grouting conditions.

The quality of the grouting can affect both the durability and the structural behavior of the PC member, the latter being the main focus of the present study. An access hole is the most reliable method for void detection, even if a number of nondestructive diagnostic tests are being studied (ANAS 2020; Nuti et al. 2020; Tonelli et al. 2020). Full grouting would provide an adequate bond between the strand and the concrete, allowing stress transfer and an increase in prestress force under external actions, especially in the postcracking response of the PC members [Fig. 1(a)]. Where the alkalinity of the grouting mortar and the surrounding concrete has been neutralized, or where the seal has been air-tight, the steel tendon will have been protected from corrosion. At $pH > 9$, however, the presence of voids around the tendons [Fig. 1(b)] would eventually compromise the full bond between the tendon and the concrete, with the bond relying on the friction at the contact surface with the duct. This has been confirmed by recent in situ inspections that have shown how injection defects can be considered on their own, and not necessarily in combination with degradation due to corrosion (ANAS 2020).

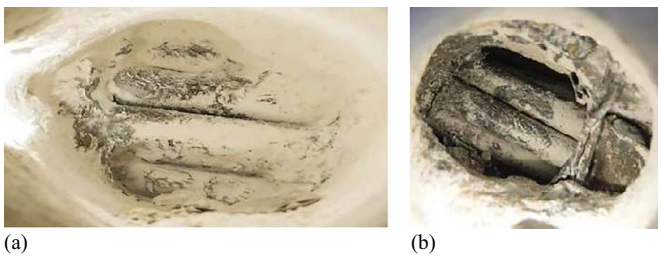

(a) (b)

Fig. 1. Visual inspection of post-tensioned tendons in a typical PC girder bridge: (a) full grouting; and (b) no grout with no corrosion effects (ANAS 2020).

The impact of residual prestress on the serviceability and ultimate behavior of existing bridges has also been addressed as a main variable that can only be estimated with a high level of uncertainty in current engineering practices (Abdel-Jaber and Glisic 2019; ANAS 2020; Tonelli et al. 2023) or with increasing costs (Frangopol et al. 2008). The prestressing level and combined internal forces can significantly affect the safety checking of PC structures (Granata and Recupero 2015; Recupero et al. 2017).

In some studies, the flexural response of either full- or reduced-scale PC bridge girders representative of existing bridges have been investigated (Deng et al. 2001), although none of these has addressed the combined influence of prestressing levels and grouting conditions on the structural behavior from serviceability to ultimate conditions (Ahlborn et al. 1997). Previous studies have shown how existing PC bridges with slight damage or deterioration overperform compared with either service or ultimate design assumptions. This understanding has recently been confirmed by an in situ collapse test of a real decommissioned PC bridge deck, the ultimate bending capacity of which was found to be almost four times the demand associated with traffic loads (Tonelli et al. 2023). In addition, a recent analytical study on a class of Italian PC girder bridge decks under code-compliant traffic loads revealed higher probabilities of failure associated with the flexural rather than shear mechanism (Miluccio et al. 2021, 2023).

To the best of the authors' knowledge, comprehensive studies are still needed to investigate the combined effects of the prestressing levels and grouting conditions of tendons in the flexural response of PC bridge girders under different levels of external action, including both their serviceability and ultimate conditions. In this paper, we present the results of an experimental campaign on six 1:5-scaled PC bridge girders with the following features: (1) two different levels of initial prestressing force—high (HP) and low (LP); and (2) three grouting conditions—full bond (B), no bond (U), and partial bond (PB). The combination of these two variables (i.e., prestressing level and grouting condition) provided a set of five defective prototpyes to compare against a benchmark prototype with an adequate prestressing level and full grouting. The influence of corrosion of, and damage to, the tendons was not considered here, as this represents a further step in our research.

Design of the Specimens

The prototype bridge was selected based on a recently decommissioned PC bridge that was deemed representative of the Italian stock in terms of its geometry and aging condition (Miluccio et al. 2021). The prototype bridge had a total length of 33 m with a classical girder deck, which was composed of precast PC I-girders connected by five reinforced concrete transverse beams and a top slab cast in situ (Tonelli et al. 2023).

In accordance with the similitude laws commonly adopted in earthquake engineering testing (Harris and Sabnis 1999; Losanno et al. 2022), the specimens were designed to a length scale of $S_L = 5$ compared with the real bridge. The main geometric features of the prototype are reported in Table 1 and shown in Fig. 2. Each specimen had a T-shaped cross-section with a 60-mm-thick slab, total depth of 440 mm, and web and top flange widths of 150

Table 1. Geometric properties of the prototype and model PC girder

Geometric property	Unit	Prototype	Model
Total length, L	Mm	33,000	6,600
Total height, H	Mm	2,200	440
Flange width, b	Mm	750	150
Slab thickness, t	Mm	300	60
Web thickness, t_w	Mm	200	150[a]
Slab effective width, b_{eff}	Mm	2,400	480
Total reinforcing steel area at the bottom level, A_s	mm^2	2,512	100
Total prestressing steel area, A_p	mm^2	7,480	299

[a]Not scaled.

and 480 mm, respectively. The total length (L) of each specimen was 6,600 mm [Fig. 2(a)]. The girder web included six longitudinal reinforcing bars in three layers (bottom, middle, top) with nominal diameters of 8 mm and a concrete cover of 30 mm. A welded wire mesh with diameter and mesh size equal to 8 mm and 200 × 200 mm^2, respectively, was embedded in the top flange. The shear reinforcement consisted of stirrups with an 8-mm nominal diameter and 100-mm longitudinal spacing to prevent the onset of shear failure mechanisms.

A web thickess greater than 40 mm (corresponding to 200 mm in the physical model) was assumed in order to properly embed the duct (external diameter of 30 mm) and the mild steel cage, ensuring proper concrete cover. The assumed web thickness for the model (150 mm) corresponded to the scaled width of the bottom flange of the I-girder (750 mm), having a larger size to embed all tendons in the midspan region. However, such a geometric distortion of the model in terms of a greater web thickness would not affect the experimental behavior due to its negligible impact on the flexural capacity.

The prestressing steel ratio was assumed based on the regression model established in Miluccio et al. (2021) and was equal to 1.0%, with the corresponding prestressing steel area determined accordingly (i.e., 300 mm^2 for the scaled model). The total prestressing steel area was provided by two monostrand tendons having 0.6′ nominal diameters (corresponding to a 15.2-mm diameter and 150-mm^2 cross-sectional area) with the shape shown in Fig. 2(a). The equivalent tendon was designed with a parabolic shape having a maximum eccentricity at the midspan, constant for a section of 1.0 m across the midspan, and zero eccentricity at the supports, avoiding the prestressing induced bending moments as per real bridges.

At the midspan cross-section, the clear depths of the upper and lower tendons (i.e., their clear distances from the top flange) were equal to 342 and 407 mm, respectively [Fig. 2(b)]. The clear depth of the upper and lower tendons reduced to 111 and 281 mm at the supports [Fig. 2(c)]. Single-strand anchorages were used at the girder end sections to restrain each tendon (DYWIDAG 2022).

The concrete mix was designed to achieve a cubic compressive strength in the range of 30 to 35 MPa after 28 curing days, which was deemed a representative value of existing top slabs cast in situ, obtained by adding 320 kg of cement per cubic meter of concrete with the aggregate sized no greater than 20 mm (Miluccio et al. 2021; Tonelli et al. 2023). For each girder, six concrete cubes were tested up to failure, providing a mean cubic compressive strength equal to 33.8 MPa. It should be noted that the compressive strength of Specimen #6 was removed from the dataset because of its higher compressive strength ($R_{\text{cm}} = 42.6$ MPa), which was deemend representative of precast concrete girders. A grouting mortar of 500 kg of cement per cubic meter, plus water and an antishrinkage additive, was injected into the ducts using a vacumm electric pump.

Tensile tests on the prestressing steel produced the following properties: Young's modulus, $E_P = 203{,}400$ MPa; conventional yield stress (i.e., the stress corresponding to the total strain equal to 1%), $f_{p1} = 1{,}782$ MPa; ultimate tensile strength, $f_{pt} = 1{,}969$ MPa. A Type B 450C mild steel was adopted, ensuring a minimum yield stress based on the Italian building code (i.e., $f_{sy} \geq 450$ MPa) (MIT 2018).

In order to set the code-conforming design values of flexural demand, a simulated design of traffic load effects was carried out on the edge girder of the real bridge. The bridge deck was analyzed under Load model 1 (LM1) of EN 1991-2 and the Italian building code (CEN 1991; MIT 2018) by adopting a simplified closed-form Courbon–Engesser formulation. The reader can refer to previous

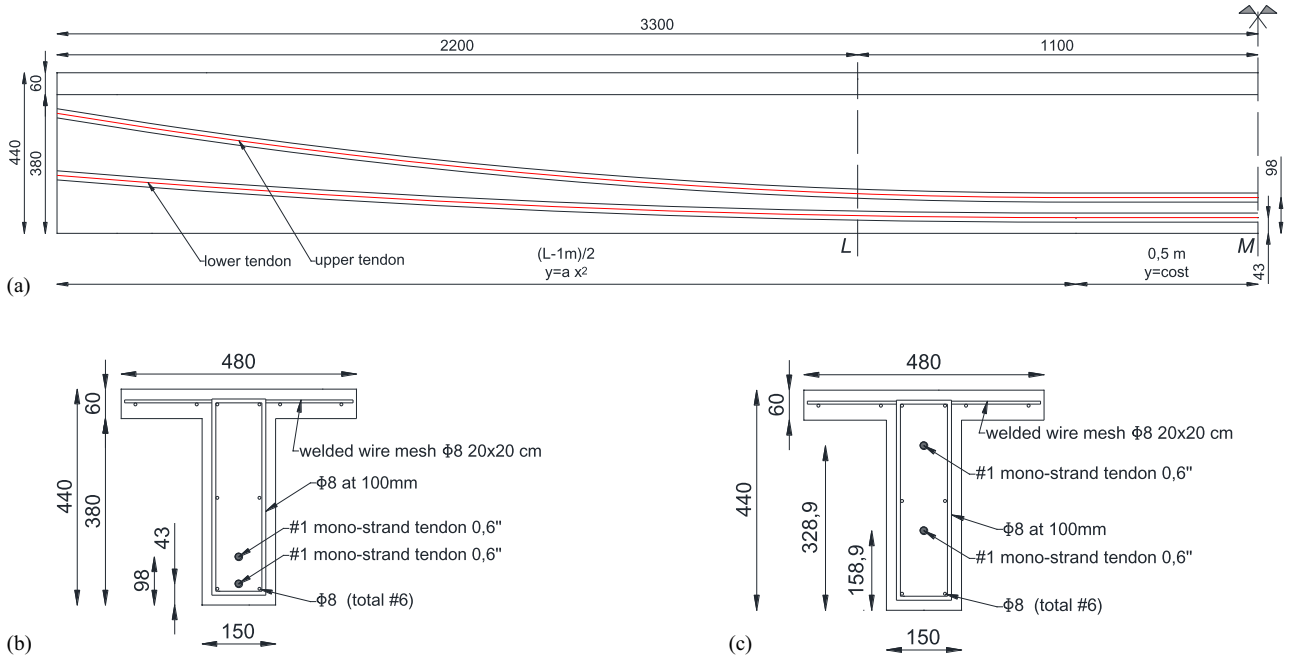

Fig. 2. (a) Side view of the half girder scaled by $S_L = 5$; (b) midspan; and (c) end cross-section (length in mm).

Table 2. Code-conforming bending moment demand (M_e)

Load combination effect	Prototype (kN · m)	Model (kN · m)
SLS	6,023	48
ULS	8,229	70
1.5 × ULS	12,343	105

studies for additional details on traffic load models and the simplified analysis for the simulated design of bridge decks (Raithel 1975; Miluccio et al. 2021).

A characteristic load combination was considered to study serviceability limit state (i.e., SLS) conditions of the bridge deck as usually assumed in a proof load test in Italy (i.e., unfactored dead plus traffic loads with their characteristic value). The combined unscaled permanent nonstructural (e.g., road pavement) and live load effects, in terms of maximum external bending moment, M_e, were calculated as equal to 6,023 kN·m on the prototype external girder. Under consistent scaling, with an elastic modulus scale factor of $S_E = 1$, the value was reduced by a factor of S_L^3 to 48 kN·m for the scaled model. The fundamental combination for ultimate limit state (i.e., ULS) safety checking was obtained by scaling maximum effects through a partial safety factor of 1.35 for live loads and self-weight and 1.50 for permanent loads, respectively (CEN 1991; MIT 2018). An additional combination, providing 1.5 times the ULS-related load intensity, was considered to investigate the performance levels involving the nonlinear behavior of the girder. The threshold values of M_e under three different load combinations for both the prototype and model edge girders are reported in Table 2.

Experimental Program

The experimental tests on six PC girders [Fig. 3(a)] are presented, including a benchmark (T1) with a high prestressing level (HP) and fully grouted tendons (B) and five additional specimens, including a lower prestressing level (LP) and/or no grouting (U) or partial grouting (PB) of the ducts. The experimental campaign was aimed at investigating the impact of prestressing and/or grouting defects on the response of different specimens with the same geometry of tendons.

Partial grouting (PB) was obtained by embedding each strand in a polyurethane jacket [Fig. 3(b)] for a total length of 1.0 m across either the midspan (M) or a lateral (L) section in the case of the girder specimens [T5 (PB-M) and T6 (PB-L), respectively]. Tendon prestressing was imposed after 28 days of concrete curing [Fig. 3(c)]. The geometry of the different specimens, in terms of grouting conditions and length of the unbonded tendons, is shown in Fig. 4. The full test matrix for the different specimens is presented in Table 3, in terms of grouting condition and jacking prestress level.

The high prestress (HP) level was obtained by imposing on each tendon a jacking stress of 1,000 MPa (i.e., $P_{target} = 150$ kN), assuming a design prestress value on the day of testing on the order of 750 MPa. Such a value was on the order of magnitude of the residual prestress in healthy existing PC bridges, assuming a maximum jacking stress equal to 80% of the yielding strength with an average of 25% of prestress losses based on standard provisions at the time of construction (Preston et al. 1975). Even if a higher residual prestress could be detected in existing bridges, a value of 750 MPa is

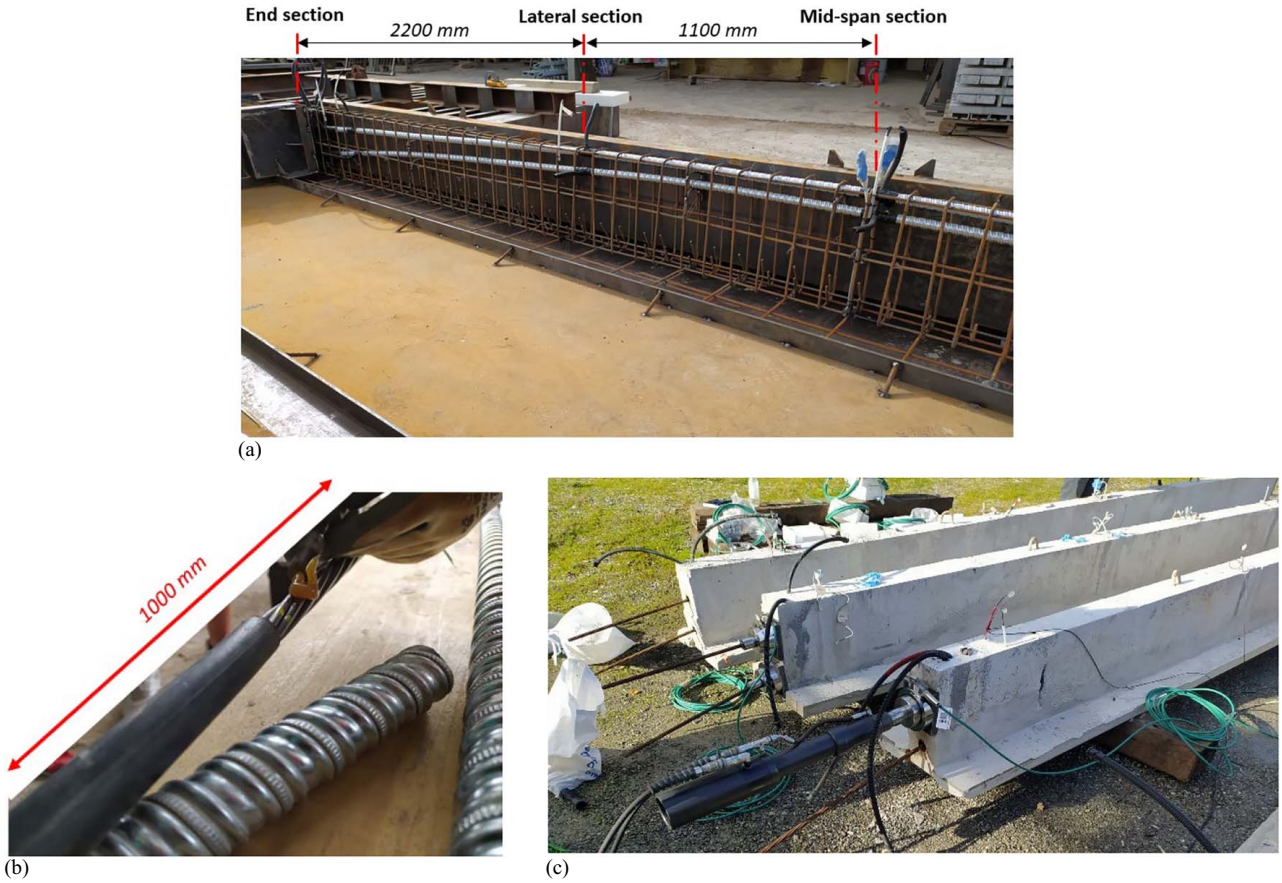

Fig. 3. (a) Side view of the upside-down girder in the steel formwork prior to casting; (b) polyurethane jacketing of 1 m of tendon for partially bonded (PB) configuration; and (c) hydraulic jack and load cells during prestressing.

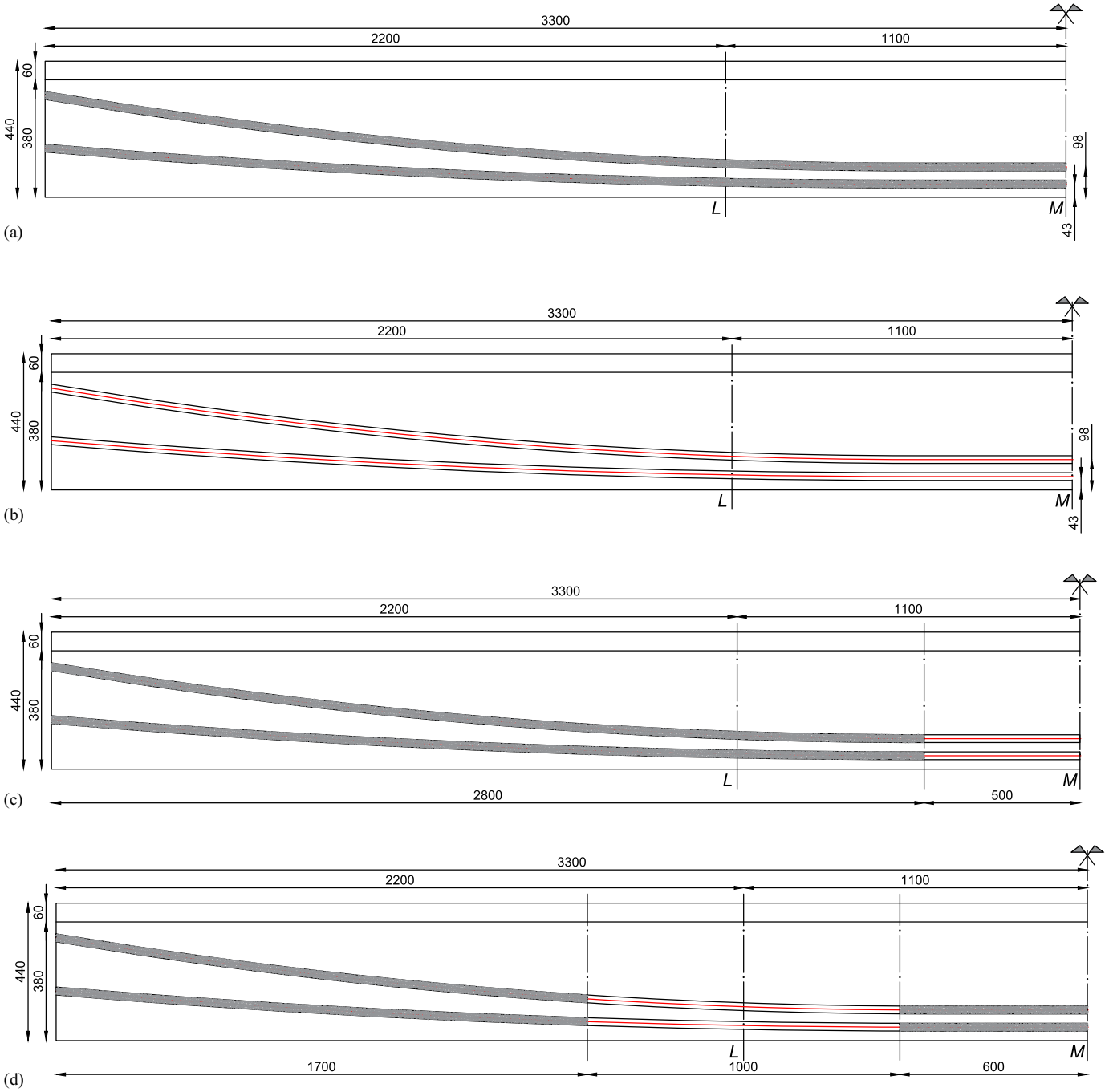

Fig. 4. Grouting conditions of the specimens: (a) full grouting (B); (b) no grouting (U); (c) unbonded tendon at the midspan (PB-M); and (d) unbonded tendon in the lateral section (PB-L).

Table 3. Specimen characteristics in terms of grouting and initial prestress level

Specimen	ID	Grouting condition	Initial prestress force
T1	B-HP	Complete (B)	150 kN (HP)
T2	U-HP	Lacking (U)	150 kN (HP)
T3	B-LP	Complete (B)	75 kN (LP)
T4	U-LP	Lacking (U)	75 KN (LP)
T5	PB-M-HP	No grouting across midspan section (PB-M)	150 kN (HP)
T6	PB-L-HP	No grouting across lateral section (PB-L)	150 kN (HP)

deemed fully representative of the case-study bridge on which a number of destructive tests were conducted, revealing a mean value of residual prestress of around 620 MPa (with a coefficient of variation of 13.5%) that is significantly lower than that originally assumed by the designer (i.e., 1,000 MPa) (Tonelli et al. 2023).

A low prestress level (LP) was imposed, limiting the jacking force to half the HP value (i.e., $P_{target} = 75$ kN), to make it representative of those bridges suffering from higher prestress losses due to, for example, more severe creep, shrinkage or steel relaxation to account for any mistake at the design or execution level. The LP condition was assumed to yield cracking under the SLS load combination.

Table 4. Prestressing force levels measured by load cells at different stages

Specimen	ID	Tendon	P_{target} (kN) [σ_{target} (MPa)]	P_i (kN) [σ_i (MPa)]	ΔP_{slip} (kN) [$\Delta\sigma_{slip}$ (MPa)]	P_{test} (kN) [σ_{test} (MPa)]	ΔP_{test} (kN) [$\Delta\sigma_{test}$ (MPa)]
T1	B-HP	Upper	150 (1,000)	124 (827)	26 (173)	104 (693)	20 (133)
		Lower		129 (860)	21 (140)	111 (740)	18 (120)
T2	U-HP	Upper	150 (1,000)	134 (893)	16 (107)	115 (767)	19 (127)
		Lower		134 (893)	16 (107)	117 (780)	17 (113)
T3	B-LP	Upper	75 (500)	48.0 (320)	27 (180)	33.4 (223)	14.6 (97.3)
		Lower		50.4 (336)	24.6 (164)	36.3 (242)	14.1 (94)
T4	U-LP	Upper	75 (500)	52.0 (347)	23 (153)	38.3 (255)	13.7 (91.3)
		Lower		52.0 (347)	23 (153)	39.2 (261)	12.8 (85.3)
T5	PB-M-HP	Upper	150 (1,000)	130 (867)	20 (133)	110 (733)	20 (133)
		Lower		130 (867)	20 (133)	112 (747)	18 (120)
T6	PB-L-HP	Upper	150 (1,000)	125 (833)	25 (167)	106 (707)	19 (127)
		Lower		109 (727)	41 (273)	92.1 (614)	16.9 (113)

The prestress level at the live end of each specimen was monitored during the different stages through either one load cell (installed on the lower tendon of T2, T4, T5, and T6) or two load cells (installed on both the upper and lower tendons of T1 and T3). Table 4 highlights the difference between the initial prestressing force (i.e., the jacking force, P_{target}), the prestressing force after instantaneous stress losses due to anchorage setting (P_i), and the residual prestressing force on the day of testing (P_{test}, i.e., the prestressing force after both the instantaneous and time-dependent losses, including creep, shrinkage, and relaxation) for the monitored tendons. The corresponding tendon stress is also reported in brackets for the sake of comparison. It should be noted that an average value of the tendon stress at testing, σ_{test}, equal to 750 and 250 MPa was reported for HP and LP, respectively, with most of the prestress losses due to wedge seating and concrete shrinkage. A slippage of 6 mm was measured in the wedges at jacking, corresponding to an average prestress loss of $\Delta\sigma_{slip} = -157$ MPa. The residual prestressing forces, P_{test}, were measured at the load cells, obtaining the total losses from prestressing to testing. These losses were due to several phenomena, including friction, concrete shrinkage, creep, and relaxation of the prestressing steel, and were estimated according to EN1992-1-1 (CEN 2004). The average prestress loss, $\Delta\sigma_{p,f}$, due to friction was –17.6 MPa and –13.0 MPa for the top and bottom tendons at the midspan cross-section, respectively, while the concrete shrinkage was taken as $\Delta\sigma_{p,s} = -75$ MPa regardless of the initial prestress level, based on Sect. 5.10.5.12 of EN1992-1-1. The average prestress loss due to steel relaxation was found to be –0.61 MPa (top tendon) and –0.63 MPa (bottom tendon), while creep was deemed to produce $\Delta\sigma_{p,c} = -13.5$ MPa (top tendon) and $\Delta\sigma_{p,c} = -15.7$ MPa (bottom tendon), on average. As can be seen, after all prestress losses, in the LP case, the value of P_{test} was approximately 30% that associated with the HP conditions. Although a value of residual prestress equal to 250 MPa is significantly lower than the actual values in most existing bridges, it can be viewed as a lower bound to those cases where prestress is still barely active, offering limited serviceability to the bridge deck under traffic loads. It is worth mentioning that, as a main difference between the target prestressing levels, the healthy (i.e., HP) and unhealthy (i.e., LP) bridge conditions were assumed not to achieve and to achieve cracking under rare combination, respectively.

Loading Protocol

Each specimen was quasi-statically tested in a four-point bending configuration to evaluate the flexural response of the PC girders. Each specimen rested on two square rubber bearings with sides measuring 150 mm, allowing any rotation at the supports. The two point loads at the midspan were spaced 850 mm apart, resulting in a shear span length measured from the bearing midpoint to the loading point of $L_v = 2{,}800$ mm. Lateral restraints were installed only to prevent parasite out-of-plane rotations and buckling, particularly under the ultimate conditions.

Fig. 5 shows the experimental setup of the tests, which were carried out in the Department of Structures for Engineering and Architecture at the University of Naples Federico II, Italy. The testing machine consisted of a rigid steel base (1.0×4.0 m^2 in plan), four columns fixed to the basement, and a moving crossbar on top, which was able to slide in the vertical direction. Based on a vertical servo-controlled hydraulic jack (actuator) placed on the crossbar, the specimens could be tested with either displacement (maximum stroke of 150 mm) or force control (compressive load capacity of 3,000 kN, tensile load capacity of 2,400 kN).

The load protocol was applied in two different phases to investigate the girder structural behavior against the code-provided external action at increasing levels (force-controlled protocol, P1) and then its response to failure (displacement-controlled protocol, P2).

During P1 (Fig. 6), the specimen was tested under six stepwise loading cycles (20 min duration per cycle) with three different increasing amplitudes of imposed vertical force, F_e (two loading cycles for each amplitude, $F_1 = 33.1$ kN for Subprotocol P1L1, $F_2 = 48.3$ kN for Subprotocol P1L2, and $F_3 = 72.4$ kN for Subprotocol P1L3) in the load-controlled mode, as per ACI 437.1R-07 (ACI Committee 437, ACI 2007). Peak force levels (F_1, F_2, F_3) were defined to impose the external bending moment, M_e, values calculated in Table 1 ($M_{e,SLS} = 48$, $M_{e,ULS} = 70$, and $M_{e,1.5xULS} = 105$ kN · m), based on the four-point loading condition, $M_e = 0.5\ F_e\ L_v$.

During P2, a displacement-controlled protocol with a constant displacement rate of 0.05 mm/s was imposed up to either girder failure or the maximum stroke of the actuator (i.e., 150 mm), whichever was reached first. In order to fail the specimens, after testing T1 and T2, additional external belts were installed to pull down the sample while resetting the full stroke of the actuator by translating its crossbar downwards.

In this paper, the response to both P1 and P2 and the complete monotonic envelope response is discussed before and after cracking, up to the maximum load, $F_{e,max}$.

Experimental Results

The girder vertical displacement at the midspan cross-section was measured using a linear variable differential transducer (LVDT)

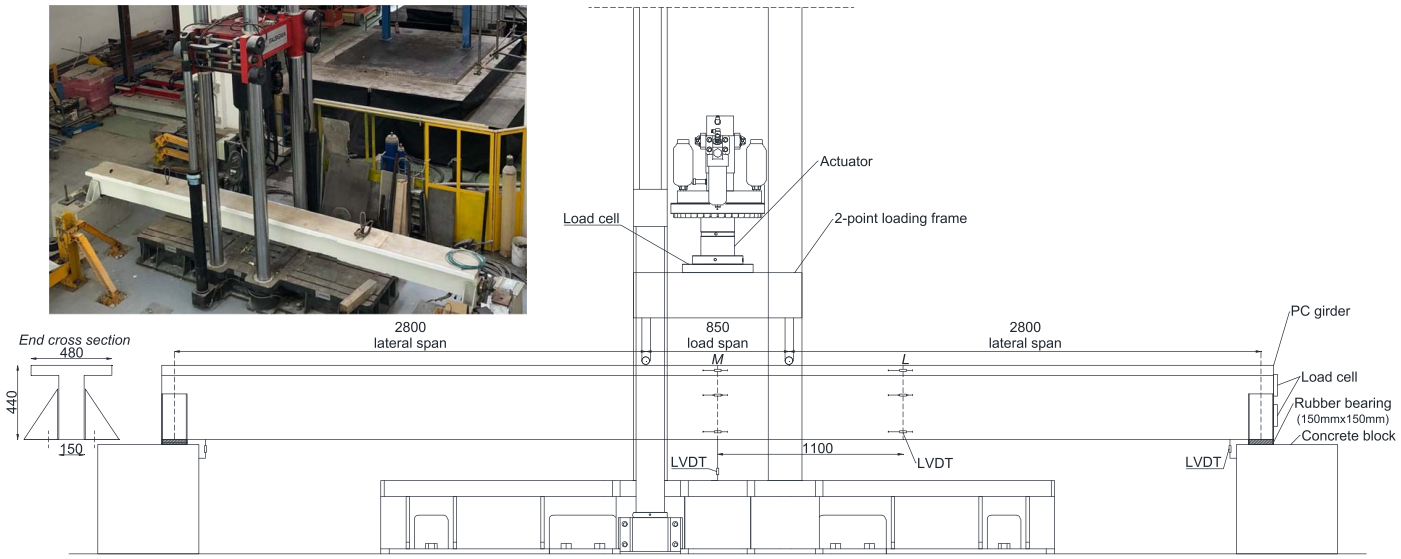

Fig. 5. Experimental setup: side view and photo of the testing apparatus.

during P1 and a potentiometer during P2, with maximum strokes of 150 and 500 mm, respectively. The midspan deflection due to the external load, d_e, was calculated as the midspan displacement measured by vertical sensors minus the displacement at the supports due to the compliance of the bearings (Fig. 5).

A load cell was used to measure the applied load, F_e (see set-up side view in Fig. 5). The variation in the prestress level in the tendons, ΔP, was monitored at the load cells to check for variation during the test. Three horizontal LVDTs were installed at the midspan (M) and in the lateral (L) cross-sections to measure the local curvature of the girder. A number of additional strain gauges and innovative capacity stress sensors, as described in La Mendola et al. (2021), were installed in the specimens to examine the local response parameters for a further study. In addition to the imposed vertical force, F_e, the corresponding maximum bending moment, M_e, is given on the secondary vertical axis of the plots referred to in the following.

Cyclic Behavior

The cyclic response of the specimens under Protocol P1 is plotted in Fig. 7. It can be seen that the LP specimens cracked under P1L1, as per the design assumption (for $F_e < F_1$), being representative of those bridges that could form cracks under traffic loads in an SLS combination. In the HP specimens, a flag-shaped hysteresis loop beyond cracking (i.e., P1L3) marked the recentering effect of the prestressing action with very limited residual displacement, regardless of the grouting condition (Vaiana and Rosati 2023). This recentering effect was less pronounced in the LP specimens, even when the unloading branch exhibited an average stiffness value between the initial stiffness and the cracked stiffness, thus ensuring limited residual deformations.

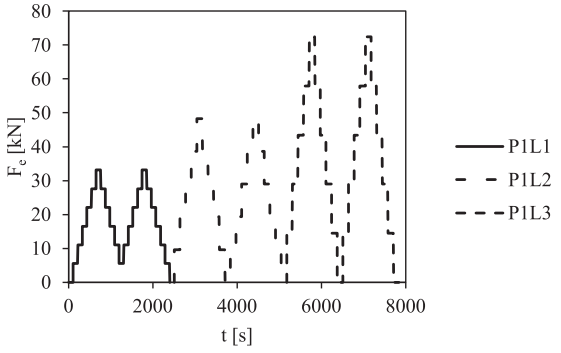

Fig. 6. Experimental protocol P1.

Beyond the cracking level, both U specimens (T2, T4) resulted in higher deformabilty (i.e., wider cracks or a higher number of cracks) compared with their B couterparts (T1, T4) due to the limited contribution of unbonded tendons to the tension stiffening. Both the T5 (PB-M-HP) and T6 (PB-L-HP) specimens provided very similar responses to the benchmark T1 in terms of cyclic response.

Fig. 8 shows the onset of cracking detected in each girder during testing. For specimens with bonded tendons, a single crack appeared at the bottom of the girder (due to the peak tensile stresses in the midspan region), as shown in Figs. 8(a and c). In the girders with unbonded or partially bonded tendons, two to three cracks were detected almost simultaneously under the same load. This could be the result of a lower tension stiffening contribution in the case of unbonded tendons.

Only in the case of T6 (PB-L-HP) did cracking initiation reflect the lack of bond in the region near the loaded span where the first cracks formed under an applied external bending moment close to the maximum value, with the tendons not being effective in providing tension stiffening.

The experimental performance was assessed through the following indices, according to ACI 437.1R-07 (ACI Committee 437, ACI 2007): (1) a repeatability index (I_R) related to the elastic recoverable deflection during two twin load cycles (Cycles A and B) at the same load level; (2) a permanency index (I_p) that measured the residual deflection compared with the corresponding maximum deflection during the second of two twin load cycles at the same load level; and (3) the I_{DL}, representing a measure of the nonlinear behavior of the structure, defined as the ratio of the slopes of two secant lines at given load levels.

$$I_R(\%) = \frac{\Delta^B_{\max} - \Delta^B_r}{\Delta^A_{\max} - \Delta^A_r} \times 100 \quad (1)$$

$$I_P(\%) = \frac{\Delta^B_r}{\Delta^B_{\max}} \times 100 \quad (2)$$

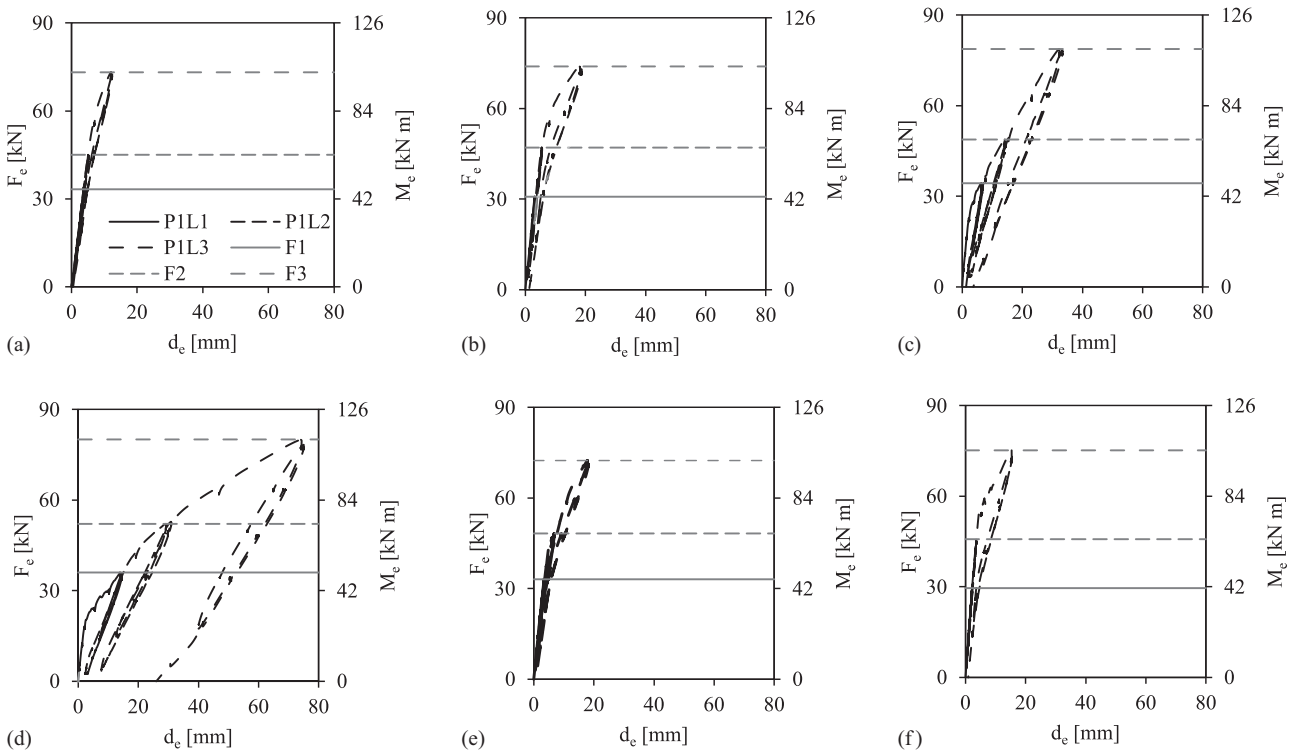

Fig. 7. Force–displacement curves under Loading protocol P1: (a) T1 (B-HP); (b) T2 (U-HP); (c) T3 (B-LP); (d) T4 (U-LP); (e) T5 (PB-M-HP); and (f) T6 (PB-L-HP).

$$I_{DL,i}(\%) = \frac{\tan \alpha_i}{\tan \alpha_{\text{ref}}} \times 100 \tag{3}$$

where $\Delta^A_{\max}$ and $\Delta^B_{\max}$ = maximum displacements attained during the first and second cycles of each load level of P1, respectively; Δ^A_r = displacement at unloading after the first cycle of each load level; Δ^B_r = displacement at the same value of vertical force of Δ^A_r; and $\tan \alpha_{\text{ref}}$ and $\tan \alpha_i$ = slopes of the the secant lines corresponding to a reference point (herein, taken as 10 kN of external force, i.e., lower than F_1) and to the ith point of the curve,

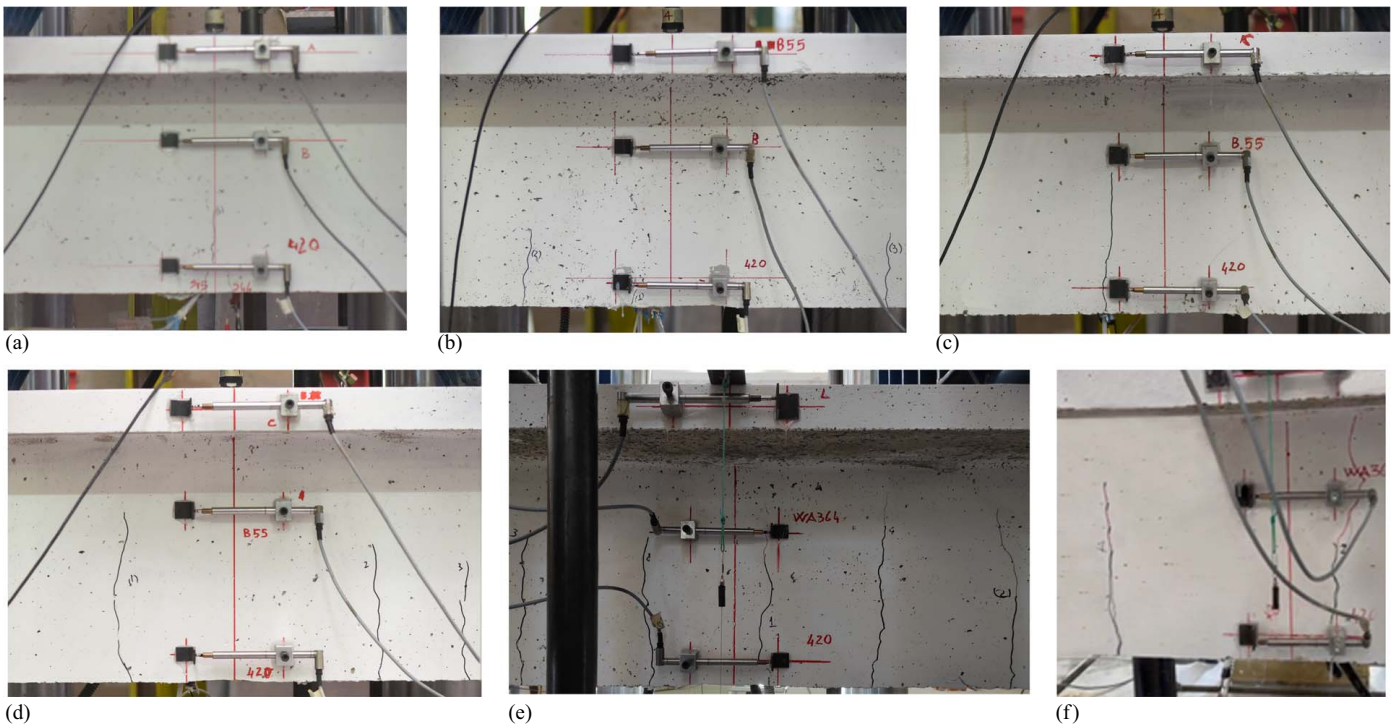

Fig. 8. Cracking of the specimens under Loading protocol P1: (a) T1 (B-HP); (b) T2 (U-HP); (c) T3 (B-LP); (d) T4 (U-LP); (e) T5 (PB-M-HP); and (f) T6 (PB-L-HP).

Table 5. Performance indexes according to ACI 437-R01

Specimen	ID	P1L1			P1L2			P1L3		
		I_R (%)	I_P (%)	I_{DL} (%)	I_R (%)	I_P (%)	I_{DL} (%)	I_R (%)	I_P (%)	I_{DL} (%)
T1	B-HP	99%	1.1%	0%	101%	1.5%	0	104%	0%	**30%**
T2	U-HP	101%	1.1%	0%	104%	0.3%	11%	105%	0%	**58%**
T3	B-LP	**113%**	2.4%	**49%**	105%	0%	**63%**	104%	0.9%	**75%**
T4	U-LP	**106%**	3.4%	**73%**	**108%**	2.8%	**81%**	100%	2.4%	**88%**
T5	PB-M-HP	102%	1.2%	2.8%	**109%**	3.4%	22%	101%	0.5%	**59%**
T6	PB-L-HP	97%	0%	4.7%	101%	0%	9.3%	100%	0%	**65%**

Note: Values exceeding acceptance limits in bold.

respectively. The obtained values for the different specimens under Protocol P1 are given in Table 5. It should be noted that the test would be passed if the I_R and I_p values were within the acceptance range of 95% to 105% and less than 10%, respectively (ACI Committee 437, ACI 2007). The index values close to the optimal values (i.e., $I_R \approx 100\%$ and $I_p \approx 0\%$) were approached by the HP specimens due to the higher cracking load and recentering action of the prestressing steel, resulting in very limited residual deformation upon unloading. Due to early cracking, the LP specimens provided values of I_R equal to 113% (T3) and 106% (T4), starting from the first two cycles at L1, offering increased flexibility under the twin cycles.

I_{DL} was severely affected by concrete cracking and was very sensitive to the grouting conditions. The deviations from linearity are plotted in Fig. 9 for each specimen, along with the acceptance limit of 25% suggested by ACI 437.1R-07 (ACI Committee 437, ACI 2007). Regarding P1L1, the deviation from linearity reached 49% and 73% only in the case of T3 (B-LP) and T4 (U-LP), respectively, with negligible values (<5%) in the HP specimens.

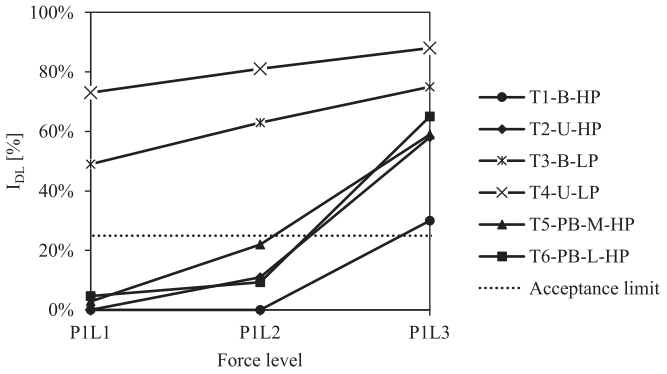

Fig. 9. Deviation from linearity under Loading protocol P1.

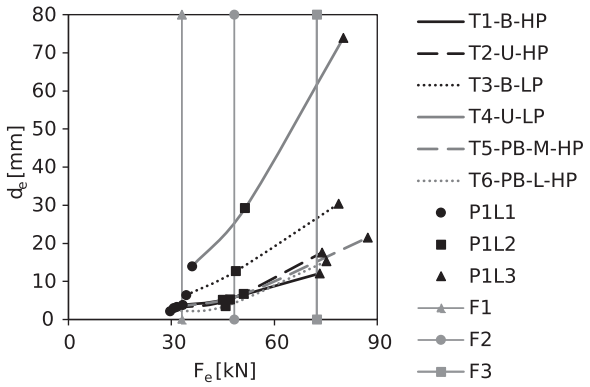

Fig. 10. Peak deflection versus peak load levels under Loading protocol P1.

Based on the three indices, it can be stated that the serviceability of the specimens was mostly affected by the prestressing level, with the influence of the grouting conditions becoming evident beyond the cracking point, when the prestressing steel could not offer adequate tension stiffening. Focusing on P1L1, the specimens performed satisfactorily in the case of HP, regardless of their grouting conditions. In the case of LP, T3 and T4 did not pass the test at SLS due to the values of I_R and I_{DL} being greater than those suggested by the ACI acceptance criteria, whereas I_p remained below 5% due to the effective recentering action of the elastic tendons.

The measured peak deflections, d_e, versus the peak levels, F_1, F_2, and F_3, are shown in Fig. 10, in which the target values of the imposed force are also plotted. During testing, slightly different values from the target (F_1, F_2, F_3) were achieved due to the significantly higher payload of the actuator compared with the imposed force levels. In the case of HP, a significant linearity was found for Specimen T1, with some increase in deformability in Specimens T2, T5, and T6 when moving from F_2 to F_3. In the case of LP, cracking was attained during P1L1 under a force level lower than F_1 (i.e., 17 kN for Specimen T3 and 20 kN for Specimen T4). In the case of the unbonded tendons (Specimen T4), the girder flexibility significanlty increased with the load, whereas, in the case of the bonded tendons (Specimen T3), intermediate displacement values between those related to Specimens T1 and T4 were obtained. Under HP conditions, cracking was either attained at the peak force level of the P1L2 stage or at any intermediate step in the P1L3 stage.

Upon the unloading of each specimen, the permanent deflection at the end of Protocol P1 was found to be approximately 1 mm for specimes with HP, and 3.50 and 26.5 mm for Specimens T3 and T4, respectively, showing a gradual increase under decreasing prestress levels and, more significantly, with a complete lack of grout. Even in the case of LP, the residual deflections tended to reduce over time due to elastic recoverable deformations in both the tendons and the reinforcing steel. In the case of the U specimens, the tendon force increments were measured at the load cells due to the significant second-order effects induced by girder vertical deflection after cracking. The peak force levels under P1L3 were found to equal 134 kN (i.e., +19 kN) and 120 kN (i.e., +82 kN) for the HP and LP conditions, respectively. Compared with the tendon yield strength, $P_{py} = 1780\ \text{MPa} \times 150\ \text{mm}^2 = 267$ kN, the peak values were limited to around 50% of P_{py}, with a fully reversible stress path and a final prestress level at the end of Protocol P1 equal to the value before testing, P_{test}. Before starting with Protocol P2, no residual deflection or open cracks were detected in any specimen.

Monotonic Behavior up to Failure

Fig. 11(a) shows the experimental response of the specimens under Protocol P2, imposed after completion of P1. It should be

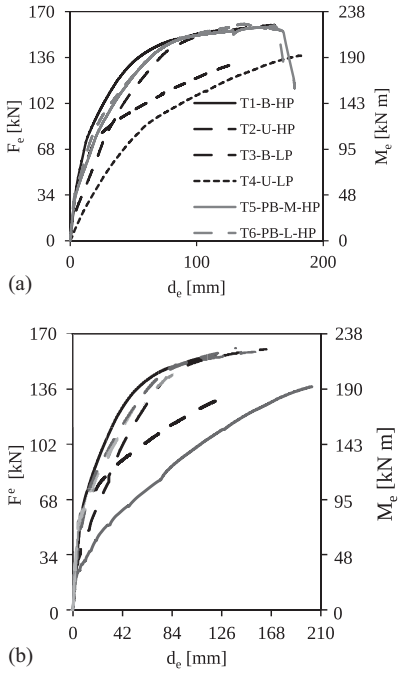

Fig. 11. Force–displacement curves: (a) test results under Loading protocol P2; and (b) monotonic envelope (P1, P2).

noted that failure conditions were only achieved in the case of Specimens T5 and T6, with softening due to concrete crushing on the top slab. Compared with the fully grouted tendons (Galano et al. 2023a), the partially bonded tendons gave rise to local effects—stress concentrations in the reanchoring section of the girder and increased compressive stress in the concrete resulting in the top slab crushing near the loading region (Galano et al. 2023b). For Specimens T1, T2, T3, and T4, a near-collapse condition was achieved due to the limited stroke of the actuator. While in the case of Specimens T1 and T3, the maximum capacity was reasonably achieved, in the case of the U specimens, a positive value of tangent stiffness at peak load provided a residual safety factor against the ultimate condition that is to be further investigated.

In the case of the B and PB specimens, the variation in tendon force at the load cell during testing was negligible (less than 1% at peak load) due to the sufficient distance between the loaded span and the end cross-section. In the case of the U specimens, the force in the tendon at the anchoring section significantly increased during Protocol P2. The rate of tendon force increase was significantly higher beyond cracking due to the increased deformability of the girder and the second-order effects resulting in additional tendon elongation. The maximum prestressing force value measured at the load cell in both U specimens achieved 240 kN. Accounting for friction losses along the metallic duct, the peak force of the tendons at the midspan were estimated at around 245 kN (i.e., around 10% lower than P_{py}).

Even if the tendon force significantly increased in the U specimens (up to 2.1 and 6 times the initial value of P_t in the case of the HP and LP conditions, respectively), higher imposed displacements would be required to fail the specimen, either in terms of concrete crusching or tensile tendon rupture. Further analytical and numerical studies of the cross-section will be developed to predict the ultimate capacity of PC girders with fully unbonded tendons with continuous voids. Table 6 provides the maximum values of $F_{e,\max}$ and $M_{e,\max}$.

Table 6. Peak values under Protocol P2

Specimen	ID	$d_{e,\max}$ (mm)	$F_{e,\max}$ (kN)	$M_{e,\max}$ (kN m)	$M_{e,\max}/M_{e,\max}^{T1}$ (−)
T1	B-HP	124	156	218	1.00
T2	U-HP	130	132	185	0.85
T3	B-LP	165	161	221	1.01
T4	U-LP	202	138	193	0.88
T5	PB-M-HP	177	159	223	1.02
T6	PB-L-HP	168	161	225	1.03

In comparing the PB and B specimens, there was a negligible difference in terms of $M_{e,\max}$ (i.e., the difference compared with T1 was less than 3%), and in the case of the unbonded tendons, the peak values were 15% to 12% lower than T1 for T2 and T4, respectively, due to the lower peak force in the tendons. It should be noted that a greater difference was obtained for T2 due to the limited imposed displacement at peak load (i.e., 130 mm compared with 200 mm in the case of T4, resulting in a 4% lower maximum bending moment). Indeed, external belts for imposing displacements larger than the actuator stroke were only installed during the tests on Specimens T3 through T6. Even if a higher level of peak bending moment could have been obtained for Specimens T2 and T4 through loading till failure, due to the positive tangent stiffness at the maximum experimental load, the load-bearing capacity of Specimen T1 can be assumed to be an upper bound for specimens with unbonded tendons. In this latter case, the bending moment capacity would be lower than that related to the bonded tendons because yielding in the prestressing steel would require very large deflections to be attained (Galano et al. 2023b).

In order to combine the P1 and P2 responses, the monotonic envelope is plotted in Fig. 11(b), in which only the load path exceeding any stress level already attained in a previous cycle is considered.

Having the same level of initial prestress, the PB specimens slightly differed from T1 only in terms of their increased flexibility in the postcracking phase due to the limited tension stiffening contribution at the cross-section with the unbonded tendons. It is worth pointing out that the B and PB specimens attained the same level of ultimate force (≈ 160 kN), this highlighting that partial grouting had little influence on the ultimate response, regardless of their initial prestressing level.

Fig. 12 shows the failure mechanism of the different prototypes representative of bonded [i.e., Specimen T3 in Fig. 12(a)], unbonded [i.e., Specimen T4 in Fig. 12(b)], and partially bonded [i.e., Specimen T5 in Fig. 12(c)] tendons. Both specimens under PB-M and PB-L conditions failed in the same zone—under the loading point close to the section corresponding to the end of the unbonded tendon between the midspan and the lateral section. In the specimens with U and PB tendons, the cracking pattern displayed wider and more-spaced cracks compared with the B-type specimens due to the unbonded tendons.

At the cross-section where the PB-L specimen failed, the concrete cover was removed and the bottom duct was opened in order to inspect the tendon that was fully grouted. In order to confirm the position of the unbonded tendon compared with the design assumptions, an additional inspection at a distance of 100 mm was carried out to check whether the tendon was bonded or not. The two inspections are reported in Fig. 13, proving that failure had occurred at the cross-section where the tendon was reanchored at the end of its unbonded length due to peak stress transfer to the cross-section. Such a local effect may explain why bending failure did not occur in the B-type Specimen T3 under the same

Fig. 12. Failure configuration of the specimens: (a) T3 (B-LP) (B); (b) T4 (U-LP); and (c) T5 (PB-M-HP).

peak displacement (i.e., around 170 mm) imposed on the partially bonded Specimens T5 and T6, which developed a softened response [Fig. 12(a)].

The following conclusions can be drawn, based on the experimental outcomes:

1. The initial stiffness is not affected by the grouting condition or the prestressing level.
2. The cracking load depends on the prestressing level regardless of the grouting condition.
3. The influence of the grouting condition becomes evident beyond the cracking point, thus resulting in higher flexibility in the unbonded as opposed to the bonded specimens, with a limited effect in partially bonded specimens.
4. Fully and partially bonded specimens reach the same peak bending moment regardless of their initial prestressing value.

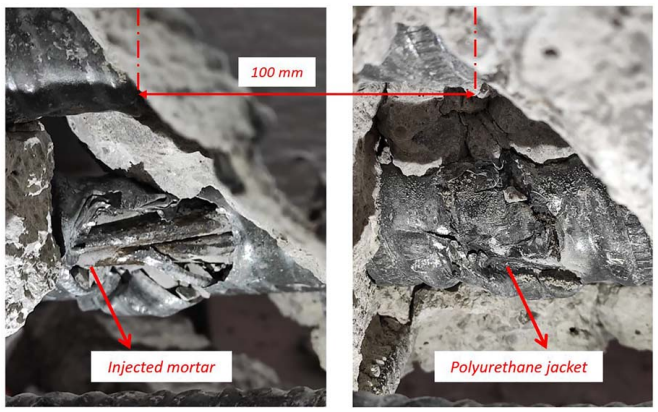

Fig. 13. Inspection of bottom tendon in Specimen T6 after failure at critical cross-section.

Table 7. Comparison between analytical and experimental values of initial vertical stiffness

Specimen	ID	K_1^{exp} (kN/mm)	$E_{cm}(t)$ (MPa)	K_1^{an} (kN/mm)	K_1^{an}/K_1^{exp} (−)
T1	B-HP	8.62	32,727	9.69	1.12
T2	U-HP	10.0	33,947	9.69	0.97
T3	B-LP	8.74	32,774	9.69	1.10
T4	U-LP	9.09	34,038	9.71	1.06
T5	PB-M-HP	9.80	33,743	9.96	1.02
T6	PB-L-HP	13.0	35,590	10.5	0.81

5. The peak load may depend on the grouting condition regardless of the prestressing level.
6. Unbonded specimens reach a lower peak bending moment than their bonded counterparts due to limited tensile force within the tendons.

Analytical Study for Test Interpretation

Calculation of Initial Vertical Stiffness

The elastic stiffness of the specimens was analyzed based on its four-point bending static scheme. Before concrete cracking, midspan deflection was obtained using the following equation:

$$d_e = \frac{F_e}{K_1} \tag{4}$$

where K_1 = vertical stiffness of the specimen. A closed-form solution for K_1 was obtained through the elastic beam theory, using the following equation:

$$K_1 = \frac{F_e}{v\left(\frac{L}{2}\right)} = \frac{F_e\, E_{cm}(t)}{\frac{L}{2}\int_0^L \frac{M_e(z)}{I_G(z)}dz - d_0^{L/2}\int_0^{L/2}\frac{M_e(z)}{I_G(z)}dz} \tag{5}$$

where $E_{cm}(t)$ = elastic modulus of the concrete on the day of testing (i.e., with t days of curing), according to EN 1992-1-1 (CEN 2004); and $I_G(z)$ = second-order moment of inertia of the generic cross-section located at z along the girder. For the bonded tendons, $I_G(z) = I_G^B(z)$ = moment of inertia accounting for variation in the position of both tendons throughout the girder. For the unbonded tendons in the cross-section, $I_G(z) = I_G^U(z)$ = moment of inertia accounting for limited prestressing steel contribution (the strands' moment of inertia with zero moment transport, i.e., $E_p\,\pi\varnothing^4/64$), acting as parallel springs within the concrete. In the partially bonded specimens, $I_G(z)$ = either $I_G^B(z)$, where the ducts were injected, or $I_G^U(z)$, where the ducts were not injected.

Table 7 shows a comparison between the experimental values of K_1 (i.e., corresponding to an external force level of 10 kN) and their analytical predictions. Considering the average values of stiffness, a good agreement was found between the experimental and analytical results, evidencing a maximum error on the order of 5%.

A simplified calculation of the vertical stiffness was also carried out, considering the gross section of concrete with no reinforcement, hence only considering I_G^c. Under such an assumption, the vertical stiffness obtained by Eq. (5) only decreased by 4% (i.e., 9.08 kN/mm), on average, and the experimental-to-numerical ratio reduced to 1.01. Limited sensitivity of the vertical stiffness to the reinforcement contribution confirmed that the uncracked response of PC girders is not affected by the grouting conditions of the tendons, and that such a defect cannot be detected at the uncracked stage, in terms of increased flexibility.

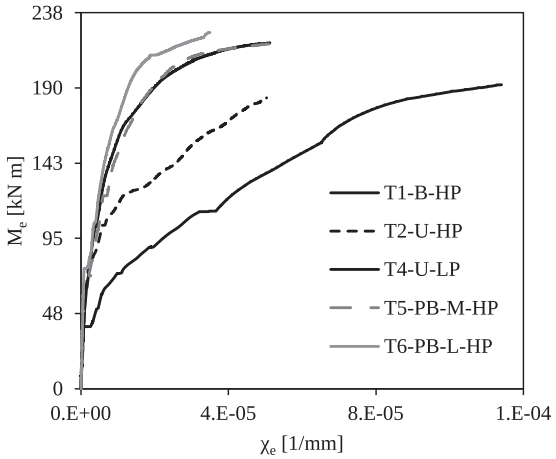

Fig. 14. Experimental envelope of moment–curvature relationships.

Moment–Curvature Analysis

The envelope of the experimental moment–curvature response at the midspan cross-section is provided in Fig. 14 for all specimens except for T3, where some measurement errors occurred at the locations of the LVDTs.

The curvature due to external loading (χ_e) was measured as follows:

$$\chi_e = \frac{\frac{\Delta L_{\text{top}}}{b_{\text{top}}} - \frac{\Delta L_{\text{bot}}}{b_{\text{bot}}}}{d_{\text{LVDT}}} \tag{6}$$

where ΔL_{top} (ΔL_{bot}) and b_{top} (b_{bot}) = displacement measure and horizontal distance, respectively, between the measurement points of the top (bottom) LVDT; and d_{LVDT} = vertical distance between them.

It should be noted that Specimen T6 outperformed Specimen T1 due to its higher concrete properties, whereas the cracking moment could easily be detected in Specimen T4 due to the LP conditions. In the HP specimens, the cracking load was not significantly lower than the yielding of the mild steel. In comparing Specimens T1 to T5, there was a perfect match, demonstrating that local curvature in the measured section was not sensitive to the unbonded tendons in Specimen T5.

An analytical study of the midspan cross-section was carried out. Based on strain compatibility (i.e., the plane sections after flexural deformation and the prestressing steel strain being the same as the concrete strain), external bending moment–curvature diagrams (i.e., excluding the girder self-weight contribution) were obtained by studying four significant force levels: (1) cracking; (2) yielding of the mild steel; (3) yielding of the prestressing steel; and (4) crushing of the concrete. A parabola–rectangle stress–strain relationship and a linear elastic stress–strain relationship up to tensile cracking were adopted for the concrete in compression and tension, respectively. The mechanical properties of the concrete (i.e., tensile strength, ultimate compressive and tensile strain) were calculated starting from the average value of the compressive strength obtained from the experimental tests on the cubic specimens (see Section 2). The concrete tensile strength was assumed according to EN1992-1-1 (CEN 2004). The prestressing steel was modeled using two different elastic–plastic constitutive laws corresponding to conventional yielding, $f_{py} = f_{p1}$ and $f_{py} = f_{pt}$, respectively, to study the influence of the tendons' strength on the ultimate capacity of the cross-section. Finally, the mild steel was modeled using the Park (Park and Paulay 1975) stress–strain model, with the strain hardening and softening based on Holzer et al. (1975).

Fig. 15 shows the experimental–analytical comparisons in terms of $M_e - \chi_e$ diagrams. It can be seen that the moment–curvature diagram for Specimen T1 was accurately predicted by the analytical model [Fig. 15(a)], both in terms of the bending moment and the corresponding curvature at cracking and yielding and under ultimate conditions. The ultimate capacity of that specimen lies between the two curves corresponding to the yielding (dashed black line) and peak (dashed gray line) tensile stress of the tendons due to hardening behavior.

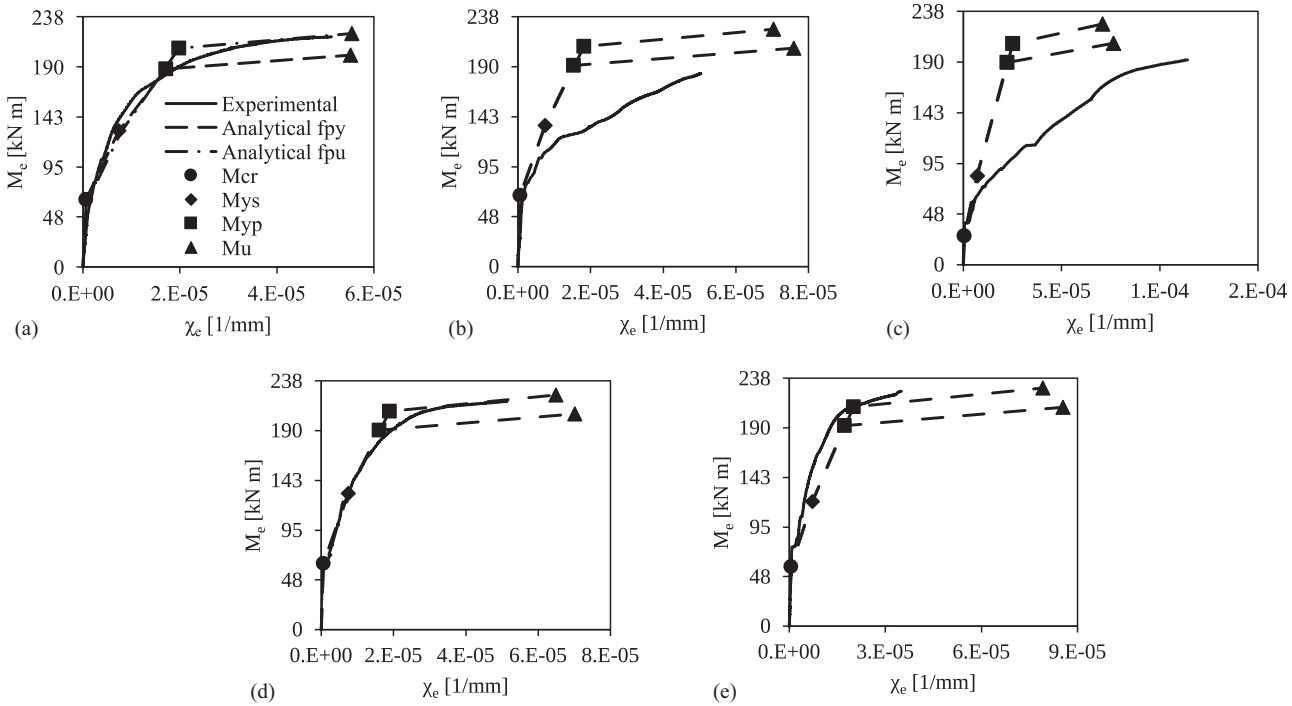

Fig. 15. Analytical moment–curvature relationships: (a) T1 (B-HP); (b) T2 (U-HP); (c) T4 (U-LP); (d) T5 (PB-M-HP); and (e) T6 (PB-L-HP).

Table 8. Analytical–experimental comparison in terms of cracking and ultimate external bending moments

		Cracking			Ultimate ($f_{py}=f_{p1}$)			Ultimate ($f_{py}=f_{pt}$)		
Specimen	ID	$M_{e,\mathrm{cr}}$ (kN m)	$M_{e,\mathrm{cr}}^{\mathrm{an}}$ (kN m)	$\frac{M_{e,\mathrm{cr}}}{M_{e,\mathrm{cr}}^{\mathrm{an}}}$ (−)	$M_{e,\max}$ (kN m)	$M_{e,u}^{f_{p1}}$ (kN m)	$\frac{M_{e,\max}}{M_{e,u}^{f_{p1}}}$ (−)	$M_{e,\max}$ (kN m)	$M_{e,u}^{f_{pt}}$ (kN m)	$\frac{M_{e,\max}}{M_{e,u}^{f_{pt}}}$ (−)
T1	B-HP	68.6	64.9	1.06	218	202	1.08	218	222	0.98
T2	U-HP	70	70.9	0.99	185[a]	208	0.89[a]	185[a]	226	0.82[a]
T3	B-LP	24.3	26.3	0.92	221	204	1.08	221	222	0.99
T4	U-LP	28	30.4	0.92	193[a]	208	0.93[a]	193[a]	226	0.85[a]
T5	PB-M-HP	62	67.8	0.91	223	207	1.08	223	224	0.99
T6	PB-L-HP	76.3	76.8	0.99	225	210	1.07	225	229	0.98
Mean		*54.9*	*56.2*	*0.97*	*222*	*207*	*1.08*	*222*	*225*	*0.99*
CoV				*6.10%*			*0.46%*			*0.77%*

Note: CoV = coefficient of variation.
[a]Not included in mean or CoV values.

The U-type specimens show very good agreement between the analytical and experimental diagrams up to cracking, (i.e., before the contribution of the tendons to sectional stiffness played a major role). Beyond cracking, the experimental curves for Specimens T2 and T4 are far below those of their analytical counterparts—under any level of imposed bending moment, the experimental response showed greater curvature than its analytical prediction, excluding the strain compatibility assumption for unbonded tendons [Figs. 15(b and c)].

Finally, both PB specimens behaved similarly to Specimen T1, even though a lower ultimate deformation capacity was observed, especially under PB-L conditions [Figs. 15(d and e)].

A comparison between the cracking and peak values of the M_e of the different specimens is summarized in Table 8. The experimental bending moment at cracking, $M_{e,\mathrm{cr}}$, was associated with a sudden increase in the bottom LVDT measured at the midspan (i.e., due to the increased flexibility of the cracked concrete in tension) along with the visual inspection of the specimen (i.e., the loading step corrisponding to Fig. 8). Even though an average percentage difference on the order of 6% was found for the full set of specimens, the experimental and analytical valus of the cracking bending moment could only approximate each other due to the indirect estimation of the concrete tensile strength.

For both the B and PB specimens, the ultimate bending moment, $M_{e,\max}$, always fell between the analytical values calculated using an elastic–plastic model, with $f_{py}=f_{p1}$ (i.e., $M_{e,u}^{f_{p1}}$) and $f_{py}=f_{pt}$ (i.e., $M_{e,u}^{f_{pt}}$), thus confirming the attainment of yielding of the bottom tendon and an ultimate strain below peak one. For the unbonded tendons, the analytical value, $M_{e,u}^{f_{p1}}$, overestimated the experimental counterpart by an average error of 9%, thus confirming the elastic behavior of the tendons. A more accurate prediction of the flexural response of the unbonded specimens is not presented in this paper as this is the subject of an ongoing study, evaluating the tension stiffening contribution and girder deformability under conditions of no grouting.

Conclusions

Here, we have presented the findings of an in-depth experimental campaign aimed at assessing the nonlinear behavior of PC girders with different prestressing levels and under different grouting conditions. Six 1:5-scaled I-girder specimens, corresponding to prototype girders representative of existing, simply supported, girder bridges built in Italy before the 1980s, were tested. Two different quasi-static protocols were imposed on each specimen, corresponding to cyclic force-controlled and monotonic displacement-controlled protocols, respectively. Increasing force levels were established according to a simulated design of the prototype girder under traffic loads, as per Eurocode Load Model 1, taking into account both its serviceability and ultimate limit states. Different performance indices were calculated for each force level, providing useful comparisons between the specimens. The specimens were then loaded to failure to evaluate their maximum bending moment capacity. The tests addressed a number of interesting features regarding the initial uncracked, cracked, and ultimate response stages of the examined PC girders.

Based on the experimental outcomes of this study, the following conclusions can be drawn:

1. The initial stiffness of the girders was not influenced by the grouting conditions, whereas the cracking load only changed with varying the initial prestressing level.
2. The recentering effect of the prestressing action upon unloading after cracking of the specimens was relevant in all cases, improving the response with very limited residual displacement.
3. The ultimate capacity of the girders with bonded tendons was not affected by the initial prestressing level.
4. In the unbonded PC girders, the prestressing force within the tendon significantly increased despite its initial value, resulting in a peak bending moment slightly lower (i.e., 12% to 15%) than that attained with fully grouted tendons. Compared with the specimens with bonded tendons, the PC girders with ungrouted tendons showed increased deformability after cracking due to limited tension stiffening.
5. Partial grouting of the ducts only resulted in slightly increased deformability of the girders after cracking, exhibiting the same flexural capacity as fully grouted tendons. These findings were confirmed by an analytical study of the cross-section, both in terms of cracking and ultimate bending moment capacity.

Based on the present study, partially grouted PC girders are not expected to suffer from any significant loss in flexural capacity compared with their fully grouted counterparts. Ungrouted PC girders need further study to evaluate their tension stiffening contribution, including the development of moment–curvature relationships to predict bending moment capacity and reduced performance levels in real bridges. A significant influence of corrosion, in terms of a progressive reduction in the effective area and a deterioration in the mechanical properties of the strands, is expected because of its potential detrimental impact on both the load and deflection capacities (Galano et al. 2023c). Therefore, future developments in this study will be focused on the effects of corrosion on the load-bearing capacity of PC girders with partially grouted and ungrouted tendons.

Data Availability Statement

All data, models, or code that support the findings of this study are available from the corresponding author upon reasonable request.

Acknowledgments

This study was developed as part of the CSLLP-ReLUIS and FIR-MITAS projects (Grant No. 2020P5572N), which were funded by the Italian High Council of Public Works and the Italian Ministry of University and Research, respectively.

Notation

The following symbols are used in this paper:

A_p = total area of prestressing steel;
A_s = total area of mild steel;
b = flange width;
b_{bot} = horizontal distance between two measuring points of the bottom LVDT;
b_{eff} = slab effective width;
b_{top} = horizontal distance between two measuring points of the top LVDT;
d_e = externally measured vertical displacement;
d_{LVDT} = vertical distance between the top and bottom LVDT;
$E_{cm}(t)$ = Young's modulus of the concrete at time t;
E_p = Young's modulus of the prestressing steel;
F_e = externally imposed vertical force;
$F_{e,max}$ = maximum value of the externally imposed vertical force;
F_1 = peak vertical force of the first level of the cyclic protocol (P1L1);
F_2 = peak vertical force of the second level of the cyclic protocol (P1L2);
F_3 = peak vertical force of the third level of the cyclic protocol (P1L3);
f_{pt} = prestressing steel ultimate tensile stress;
f_{py} = analytical yield stress of the prestressing steel;
f_{p1} = prestressing steel tensile stress at 1% of total deformation;
f_{sy} = yielding stress of the mild steel;
H = total height of the specimens;
$I_G^B(z)$ = second-order moment of inertia of the girder cross-section with bonded tendons;
I_{DL} = deviation from linearity index;
$I_G(z)$ = second-order moment of inertia of the girder cross-section;
I_R = repeatability index;
$I_G^U(z)$ = second-order moment of inertia of the girder cross-section with unbonded tendons;
I_G^c = second-order moment of inertia of the girder gross-section;
I_p = permanency index;
K_1 = precracking vertical stiffness of the girder;
L = total length of the specimens;
M_e = bending moment due to external loading;
$M_{e,SLS}$ = bending moment related to the serviceability limit state;
$M_{e,ULS}$ = bending moment related to the ultimate limit state;
$M_{e,max}$ = maximum value of the bending moment due to external loading;
$M_{e,1.5xULS}$ = bending moment related to 1.5 x the ultimate limit state;
$M_{e,u}^{f_{pt}}$ = analytical bending moment calculated assuming $f_{py} = f_{pt}$;
$M_{e,u}^{f_{p1}}$ = analytical bending moment calculated assuming $f_{py} = f_{p1}$;
P_i = prestressing force after instantaneous losses;
P_{py} = tendon yield strength corresponging to f_{py};
P_{target} = initial prestressing force;
P_{test} = prestressing force after instantaneous and time-dependent losses;
R_{cm} = mean cubic strength of concrete;
S_E = elastic modulus scale factor;
S_L = length scale factor;
t = slab thickness;
t_w = web thickness;
ΔP = variation of the prestressing force;
Δ_{bot} = horizontal displacement of the bottom LVDT;
Δ_{top} = horizontal displacement of the top LVDT;
σ_{test} = prestress at the time of testing;
$\varnothing$ = equivalent diameter of the prestressing tendon; and
χ_e = curvature due to external loading.

References

Abdel-Jaber, H., and B. Glisic. 2019. "Monitoring of prestressing forces in prestressed concrete structures—An overview." *Struct. Control Health Monit.* 26 (8): e2374.

ACI (American Concrete Institute). 2007. *Load tests of concrete structures: Methods, magnitude, protocols, and acceptance criteria*. ACI 437-07. Farmington Hills, MI: ACI.

Ahlborn, T. M., C. K. Shield, and C. W. French. 1997. "Full-scale testing of prestressing concrete bridge girder." *Exp. Tech.* 21: 33–35. https://doi.org/10.1111/j.1747-1567.1997.tb00490.x.

Alampalli, S., D. M. Frangopol, J. Grimson, M. W. Halling, D. E. Kosnik, E. O. L. Lantsoght, D. Yang, and Y. E. Zhou. 2021. "Bridge load testing: State-of-the-practice." *J. Bridge Eng.* 26 (3): 03120002. https://doi.org/10.1061/(asce)be.1943-5592.0001678.

ANAS (Azienda Nazionale Autonoma delle Strade Statali). 2020. *Ispezioni approfondita di impalcati da ponte con travi da ponte in c.a.p. a cavi post-tesi*. [In Italian.] Roma: Centro Sperimentale Stradale di Cesano.

Anitori, G., J. R. Casas, and M. Ghosn. 2013. "Redundancy and robustness in the design and evaluation of bridges: European and North American perspectives." *J. Bridge Eng.* 18 (12): 1241–1251. https://doi.org/10.1061/(asce)be.1943-5592.0000545.

Borzi, B., P. Ceresa, P. Franchin, F. Noto, G. M. Calvi, and P. E. Pinto. 2015. "Seismic vulnerability of the Italian roadway bridge stock." *Earthquake Spectra* 31 (4): 2137–2161. https://doi.org/10.1193/070413EQS190M.

CEN (European Committee for Standardization). 1991. *Actions on structures—Part 2: Traffic loads on bridges*. EN 1991-2: Eurocode 1. Brussels, Belgium: CEN.

CEN (European Committee for Standardization). 2004. *Design of concrete structures—Part 1-1: General rules and rules for buildings*. EN 1992-1-1: Eurocode 2. Brussels, Belgium: CEN.

Chen, S.-Z., G. Wu, D.-C. Feng, Z. Wang, and X.-Y. Cao. 2020. "Multi-cross-reference method for highway-bridge damage identification based on long-gauge fiber Bragg-grating sensors." *J. Bridge Eng.* 25 (6): 04020023. https://doi.org/10.1061/(asce)be.1943-5592.0001542.

Cook, W., P. J. Barr, and M. W. Halling. 2015. "Bridge failure rate." *J. Perform. Constr. Facil.* 29 (3): 04014080. https://doi.org/10.1061/(asce)cf.1943-5509.0000571.

Cosenza, E., and D. Losanno. 2021. "Assessment of existing reinforced-concrete bridges under road-traffic loads according to the new Italian guidelines." *Struct. Concr.* 22 (5): 2868–2881. https://doi.org/10.1002/suco.202100147.

Deng, L., M. Ghosn, A. Znidaric, and J. R. Casas. 2001. "Nonlinear flexural behavior of prestressed concrete girder bridges." *J. Bridge Eng.*

6 (4): 276–284. https://doi.org/10.1061/(ASCE)1084-0702(2001)6:4(276).
Deng, L., W. Wang, and Y. Yu. 2016. "State-of-the-art review on the causes and mechanisms of bridge collapse." *J. Perform. Constr. Facil.* 30 (2): 04015005. https://doi.org/10.1061/(asce)cf.1943-5509.0000731.
DOT. 2013. *Guidelines for sampling, assessing, and restoring defective grout in prestressed concrete bridge post-tensioning ducts*. Washington, DC: DOT.
DYWIDAG (Dyckerhoff & Widmann AG). 2022. *Bonded post-tensioning systems using strands*. Munich, Germany: DYWIDAG.
fib (Fédération internationale du béton). 2001. *Durability of post-tensioning tendons*. fib Bulletins 15. Ghent, Belgium: *fib*.
Franceschini, L., F. Vecchi, B. Belletti, C. Andrade, and H.-C. Peiretti. 2022. "Analytical method for the evaluation of the residual service life of prestressed concrete beams subjected to corrosion deterioration." *Struct. Concr.* 23 (1): 121–137. https://doi.org/10.1002/suco.202100245.
Frangopol, D. M., F. Asce, A. Strauss, and S. Kim. 2008. "Bridge reliability assessment based on monitoring." *J. Bridge Eng.* 13 (3): 258–270. https://doi.org/10.1061/ASCE1084-0702200813:3258.
Galano, S., D. Losanno, G. Miluccio, and F. Parisi. 2023a. "Multidimensional nonlinear numerical simulation of post-tensioned concrete girders with different prestressing levels." *Struct. Concr.* https://doi.org/10.1002/suco.202300272.
Galano, S., D. Losanno, and F. Parisi. 2023b. "Experimental and numerical evaluation of the flexural response of post-tensioned concrete girders with different prestressing levels and grouting conditions." *Eng. Struct.*
Galano, S., S. Ravasini, L. Franceschini, D. Losanno, B. Belletti, F. Parisi, and S. Aida. 2023c. "Numerical simulations of a benchmark reduced-scale post-tensioned concrete bridge girder with corroded strands." In *Proc., Capacity Assessment of Corroded Reinforced Concrete Structures: From Research to Daily Engineering Evaluation*. Hoboken, NJ: John Wiley & Sons, Inc.
Gino, D., P. Castaldo, G. Bertagnoli, L. Giordano, and G. Mancini. 2020. "Partial factor methods for existing structures according to *fib* Bulletins 80: Assessment of an existing prestressed concrete bridge." *Struct. Concr.* 21 (1): 15–31. https://doi.org/10.1002/suco.201900231.
Granata, M. F., and A. Recupero. 2015. "Serviceability and ultimate safety checks of segmental concrete bridges through N-M and M-V interaction domains." *J. Bridge Eng.* 20 (8): B4014003. https://doi.org/10.1061/(asce)be.1943-5592.0000686.
Granata, M. F., A. Recupero, G. Culotta, and M. Arici. 2021. "Influence of axial force and corrosion on failure of prestressed concrete structures considering M-V interaction." *Eng. Struct.* 242: 112552. https://doi.org/10.1016/j.engstruct.2021.112552.
Harries, K. A. 2009. "Structural testing of prestressed concrete girders from the Lake View Drive Bridge." *J. Bridge Eng.* 14 (2): 78–92. https://doi.org/10.1061/ASCE1084-0702200914:278.
Harris, H. G., and G. M. Sabnis. 1999. "Engineering & technology, mathematics & statistics." In *Structural modeling and experimental techniques*, edited by T. Pletsher, and C. Whitehead, 808. Boca Raton, FL: CRC Press.
Holzer, S. M., R. J. Melash, R. M. Barker, and A. E. Somers. 1975. *Singer: A computer code for general analysis of two-dimensional reinforced concrete structures*. Blacksburg, VA: Defense Technical Information Center.
La Mendola, L., M. C. Oddo, M. Papia, F. Pappalardo, A. Pennisi, G. Bertagnoli, F. Di Trapani, A. Monaco, F. Parisi, and S. Barile. 2021. "Performance of two innovative stress sensors imbedded in mortar joints of new masonry elements." *Constr. Build. Mater.* 297: 123764. https://doi.org/10.1016/j.conbuildmat.2021.123764.
Losanno, D., A. Calabrese, I. E. Madera-Sierra, M. Spizzuoco, J. Marulanda, P. Thomson, and G. Serino. 2022. "Recycled versus natural-rubber fiber-reinforced bearings for base isolation: Review of the experimental findings." *J. Earthquake Eng.* 26 (4): 1921–1940. https://doi.org/10.1080/13632469.2020.1748764.
Miluccio, G., D. Losanno, F. Parisi, and E. Cosenza. 2021. "Traffic-load fragility models for prestressed concrete girder decks of existing Italian highway bridges." *Eng. Struct.* 249: 113367. https://doi.org/10.1016/j.engstruct.2021.113367.
Miluccio, G., D. Losanno, F. Parisi, and E. Cosenza. 2023. "Fragility analysis of existing prestressed concrete bridges under traffic loads according to new Italian guidelines." *Struct. Concr.* 24 (1): 1053–1069. https://doi.org/10.1002/suco.202200158.
Minh, H., H. Mutsuyoshi, and K. Niitani. 2007. "Influence of grouting condition on crack and load-carrying capacity of post-tensioned concrete beam due to chloride-induced corrosion." *Constr. Build. Mater.* 21 (7): 1568–1575. https://doi.org/10.1016/j.conbuildmat.2005.10.004.
MIT (Ministero delle Infrastrutture e dei Trasporti). 2018. *Decreto 17/01/2008 - Aggiornamento delle "Norme tecniche per le costruzioni."* [In Italian.]. Rome, Italy: Gazzetta Ufficiale della Repubblica Italiana.
MIT (Ministero delle Infrastrutture e dei Trasporti). 2019. *Linee guida per la classificazione e gestione del rischio, la valutazione della sicurezza ed il monitoraggio dei ponti esistenti*. [In Italian.] Rome: MIT.
Nuti, C., B. Briseghella, A. Chen, D. Lavorato, T. Iori, and I. Vanzi. 2020. "Relevant outcomes from the history of Polcevera Viaduct in Genova, from design to nowadays failure." *J. Civ. Struct. Health Monit.* 10 (1): 87–107. https://doi.org/10.1007/s13349-019-00371-6.
Park, R., and T. Paulay. 1975. *Reinforced concrete structures*. New York: Wiley.
Preston, H. K., et al. 1975. "Recommendations for estimating prestress losses." *PCI J.* 1975: 43–75.
Raithel, A. 1975. *Ponti a travata*. [In Italian.]. Naples, Italy: Liguiri Editore.
Recupero, A., M. F. Granata, G. Culotta, and M. Arici. 2017. "Interaction between longitudinal shear and transverse bending in prestressed concrete box girders." *J. Bridge Eng.* 22 (1): 04016107. https://doi.org/10.1061/(asce)be.1943-5592.0000990.
Recupero, A., and N. Spinella. 2019. "Experimental tests on corroded prestressed concrete beams subjected to transverse load." *Struct. Concr.* 20 (6): 2220–2229. https://doi.org/10.1002/suco.201900242.
Tonelli, D., M. Luchetta, F. Rossi, P. Migliorino, and D. Zonta. 2020. "Structural health monitoring based on acoustic emissions: Validation on a prestressed concrete bridge tested to failure." *Sensors* 20 (24): 7272. https://doi.org/10.3390/s20247272.
Tonelli, D., F. Rossi, F. Brighenti, A. Verzobio, A. Bonelli, and D. Zonta. 2023. "Prestressed concrete bridge tested to failure: The Alveo Vecchio Viaduct case study." *J. Civ. Struct. Health Monit.* 13: 873–899. https://doi.org/10.1007/s13349-022-00633-w.
Trejo, D., R. Pillai, M. Beth, D. Hueste, and P. Gardoni. 2009. "Parameters influencing corrosion and tension capacity of post-tensioning strands." *ACI Mater. J.* 106-M18: 144–153.
Vaiana, N., and L. Rosati. 2023. "Classification and unified phenomenological modeling of complex uniaxial rate-independent hysteretic responses." *Mech. Syst. Sig. Process.* 182: 109539. https://doi.org/10.1016/j.ymssp.2022.109539.
Vecchi, F., L. Franceschini, F. Tondolo, B. Belletti, J. Sánchez Montero, and P. Minetola. 2021. "Corrosion morphology of prestressing steel strands in naturally corroded PC beams." *Constr. Build. Mater.* 296: 123720. https://doi.org/10.1016/j.conbuildmat.2021.123720.
VSL International. 2002. *Grouting of post-tensioning tendons - 5 VSL report series introduction*. Bern, Switzerland: VSL International.
Wang, L., X. Zhang, J. Zhang, Y. Ma, Y. Xiang, and Y. Liu. 2014. "Effect of insufficient grouting and strand corrosion on flexural behavior of PC beams." *Constr. Build. Mater.* 53: 213–224. https://doi.org/10.1016/j.conbuildmat.2013.11.069.
Wardhana, K., F. C. Hadipriono, and F. Asce. 2003. "Analysis of recent bridge failures in the United States." *J. Perform. Constr. Facil.* 17 (3): 144–150. https://doi.org/10.1061/ASCE0887-3828200317:3144.
Xu, J.-G., D.-C. Feng, and G. Wu. 2021. "Life-cycle performance assessment of aging bridges subjected to tsunami hazards." *J. Bridge Eng.* 26 (6): 04021025. https://doi.org/10.1061/(ASCE).